European Congress on Computational Methods in Applied Sciences and Engineering
ECCOMAS 2000
Barcelona, 11-14 September 2000

IMPLEMENTATION AND ASSESSMENT OF LOW-REYNOLDS TURBULENCE MODELS FOR AIRFOIL FLOWS ON UNSTRUCTURED GRIDS

D. G. Koubogiannis[⋆] and K. C. Giannakoglou[†]

[⋆] National Technical University of Athens (NTUA) P.O. Box 64069, 15710, Athens, Greece e-mail: dkoumbog@central.ntua.gr

[†] National Technical University of Athens (NTUA) P.O. Box 64069, 15710, Athens, Greece e-mail: kgianna@central.ntua.gr

Key words: Unstructured grids, low-Reynolds turbulence models, transition modelling, subsonic high-lift flows.

Abstract. *Three low-Reynolds turbulence models are implemented in an unstructured-grid, Navier-Stokes, finite-volume solver. These are the one-equation model of Spalart-Allmaras, the Shear-Stress-Transport $k-\omega$ model and a hybrid one/two-equation $k-\varepsilon$ model. All of them are shown to be robust and compliant with unstructured grids. They are used to numerically predict the subsonic flow around two-dimensional high-lift configurations, namely the two-element NLR-7301 airfoil and the single-element A-airfoil, where turbulent separation occurs near the trailing edge at high incidence angles. Both global coefficient distributions (C_p, C_f, C_l, C_d) and local boundary layer quantities or velocity profiles are compared with measured data. Due to the very stretched grid cells used close to solid boundaries, the definition of the finite-volumes (median-dual or containment circle-dual tesselation of the domain) is crucial for the quality of the results. Besides, the effect of including or not a transition mechanism into the turbulence model is investigated. The results from all models are satisfactory; the Spalart-Allmaras model performs slightly better than the other two models in terms of both predictive capability and numerical robustness.*

1 INTRODUCTION

In aerodynamic flows, one- and two-equation turbulence models have credited certain advantages. Despite their simplicity, their numerical stability outperforms that of other more sophisticated models often producing results of comparable quality. However, they are not always free of convergence difficulties due to the stiff low-Reynolds terms employed in the vicinity of solid walls and these require particular treatment. The numerical implementation of such models on structured grids is straightforward. Transverse grid lines are purposely made quasi-orthogonal to the solid boundaries, so that either distances from the wall or derivatives of flow quantities normal to the wall are computed accurately. For this reason, models such as those of Launder-Sharma [1], Chien [2], etc. have been widely used with structured grids.

During the last years, there has been a substantial progress made in the use of finite-volume techniques on unstructured grids for the solution of flow problems in complex geometries. Upwind schemes based on one-dimensional approximate Riemann solvers of second order accuracy [3], [4] or even equivalent "central schemes" with artificial dissipation [5], [6] are usually employed for the discretization of the inviscid terms. With regard to turbulence modelling for unstructured grids, most of the available works rely on the use of algebraic eddy-viscosity models [7], [8] or differential models based on the wall functions technique [9], [10], [11]. There are a few papers which employ low-Reynolds two-equation models on unstructured grids [9], [12]. The Spalart-Allmaras [13] or the Baldwin-Barth [14] one-equation models are used in preference to other models [15], [16].

In the present work, three low-Reynolds eddy-viscosity models (a one-, a two-equation and a hybrid one/two-equation model) are employed in a primitive variable, finite-volume Navier-Stokes solver for unstructured grids. Their straightforward implementation results to convergence difficulties and, in some cases, lowers the results accuracy. The latter is a consequence of using very stretched grid cells close to the solid boundaries. To increase accuracy, an alternative to the usual definition of the control-volumes [3] is adopted and tested. For the same reason, the least-squares gradient approximation for the MUSCL scheme is used. Convergence is enhanced through the linearization of the models' source terms. The inclusion of a laminar-to-turbulent transition mechanism is investigated using the one-equation model. The flow problems used to evaluate the relevant software are the two-element NLR-7301 configuration and the ONERA A-airfoil.

2 TURBULENCE MODELLING

In what follows, the three turbulence models used, are briefly described. For detailed explanation of the appearing terms, quantities and constant values, the reader should refer to the cited original publications.

2.1 Spalart-Allmaras One-Equation Model (SA)

The SA model [13] is one of the most successful one-equation models. It solves a single differential equation in terms of $\tilde{\mu}$, from which the turbulent viscosity coefficient is derived. Its compressible flow variant reads

$$\frac{\partial(\rho\tilde{\mu})}{\partial t}+\frac{\partial(\rho u\tilde{\mu})}{\partial x}+\frac{\partial(\rho v\tilde{\mu})}{\partial y}=\mathrm{Diff}_{SA}+S_{SA}\ \ ,\ \ \mu_t=\mathrm{Re}f_{v1}\tilde{\mu} \tag{1}$$

$$\mathrm{Diff}_{SA}=\frac{1}{\mathrm{Re}}\frac{1}{\sigma}\left[(1+c_{b2})\nabla\cdot((\mu+\tilde{\mu})\nabla\tilde{\mu})\ -c_{b2}(\mu+\tilde{\mu})\nabla\cdot(\nabla\tilde{\mu})\right] \tag{2}$$

$$S_{SA}=\left[(1-f_{t2})c_{b1}\rho\tilde{S}\tilde{\mu}-\frac{1}{\mathrm{Re}}(c_{w1}f_w-\frac{c_{b1}}{\kappa^2}f_{t2})\left(\frac{\tilde{\mu}}{d}\right)^2\right]+\mathrm{Re}f_{t1}\Delta U^2 \tag{3}$$

Transition trip is included in the coefficients f_{t1} and f_{t2} which depend upon the distance from the transition point. If such a point is not defined, these coefficients should be zeroed. Along solid walls μ_t is set to zero. At the inlet, the turbulent viscosity is set equal to 0.01μ, μ being the molecular viscosity.

2.2 Shear-Stress-Transport $k-\omega$ Model (SST)

The SST $k-\omega$ model has been introduced in [17] as an extension of a blended $k-\varepsilon$ /$k-\omega$ model and is considered to be the state-of-the-art $k-\omega$ model. The model equations in conservative vector form read

$$\frac{\partial\mathbf{W}_t}{\partial t}+\frac{\partial\mathbf{F}_t}{\partial x}+\frac{\partial\mathbf{G}_t}{\partial y}=\mathbf{S}_t \tag{4}$$

where $\mathbf{W}_t=(\rho k,\ \rho\omega)^T$, $\mathbf{F}_t=\mathbf{F}_t^{inv}-\mathbf{F}_t^{vis}$ (the same for $\mathbf{G}$) and $\mathbf{S}_t=(S_k,\ S_\omega)^T$, where

$$S_k=P_k-\beta^*\rho k\omega\ \ ,\ \ S_\omega=\gamma\frac{\rho\mathrm{Re}}{\mu_t}P_k-\beta\rho\omega^2+2\rho(1-F_1)\sigma_{\omega2}\frac{1}{\omega}\nabla k\cdot\nabla\omega \tag{5}$$

$$F_1=\tanh\left(\mathrm{arg}_1^4\right)\ \ ,\ \ \mathrm{arg}_1=\min\left\{\max\left(\frac{\sqrt{k}}{\beta^*\omega d}\ ;\ \frac{500\mu}{\mathrm{Re}\rho\omega d^2}\right)\ ;\ \frac{4\rho\sigma_{\omega2}k}{C_{k\omega}d^2}\right\} \tag{6}$$

$$C_{k\omega}=\max\left(2\rho\sigma_{\omega2}\frac{1}{\omega}\nabla k\cdot\nabla\omega\ ;\ 10^{-20}\right)\ \ ,\ \ \mu_t=\frac{a_1\rho k}{\max(a_1\omega\ ;\ \Omega F_2)} \tag{7}$$

$$F_2=\tanh\left(\mathrm{arg}_2^2\right)\ \ ,\ \ \mathrm{arg}_2=\max\left(2\sqrt{k}/\beta^*\omega d\ ;\ 500\mu/\mathrm{Re}\rho\omega d^2\right) \tag{8}$$

Model constants is computed by the linear combination $\mathcal{S}=\mathcal{S}_1\Phi_1+(1-F_1)\mathcal{S}_2$, where $\mathcal{S}_i=\{\beta_i,\sigma_{\omega i},\sigma_{ki},\gamma_i\}$, $\mathcal{S}_1=\{0.075,\ 0.5,\ 0.85,\ 0.55\}$, $\mathcal{S}_2=\{0.0828,\ 0.856,\ 1.0,\ 0.44\}$.

The wall boundary conditions are $k_w=0$ and $\omega_w=60\mu/\mathrm{Re}\rho\beta d_w^2$, where d_w is the distance of the first node off the wall [17]. For each wall node we define d_w to be equal to

the mean value of the heights of the (two) triangles lying on the wall and sharing this node. At inflow, $\omega_{in} = 10V_{in}/L$, L being the computational domain length and $k_{in} = \alpha\mu\omega/\mathrm{Re}$ with $\alpha = \mu_t/\mu = 0.01$.

2.3 Two-Layer $k-\varepsilon$ Model (TLKE)

The TLKE model is a $k-\varepsilon$ variant, which consists, in its main part, of the standard high-Reynolds $k-\varepsilon$ model [18], which is written as in equation 4 with $\mathbf{W}_t = (\rho k,\ \rho\varepsilon)^T$ and $S_k = P_k - D_k$, $S_\varepsilon = c_{\varepsilon 1}P_k\varepsilon/k - c_{\varepsilon 2}\rho\varepsilon^2/k$, $D_k = \rho\varepsilon$, $c_{\varepsilon 1} = 1.44$, $c_{\varepsilon 2} = 1.92$, $c_\mu = 0.09$, $\sigma_k = 1.0$, $\sigma_\varepsilon = 1.3$. Close to the wall, the one-equation model of Wolfsthein [19] is used instead. This is based upon the same equation for k with $D_k = (\rho\varepsilon)_{1eq}$, an algebraic relation for ε and a different definition of the turbulent viscosity. Thus $D_k = (\rho\varepsilon)_{1eq} = \rho k^{3/2}/l_\varepsilon$ and $\mu_t = \rho c_\mu l_\mu\sqrt{k}\mathrm{Re}$. The involved length scales $l_\mu = \kappa {c_\mu}^{-3/4} d[1-\exp(-d^+/70)]$ and $l_\varepsilon = \kappa {c_\mu}^{-3/4} d[1-\exp(-d^+/(2\kappa {c_\mu}^{-3/4})]$ with $d^+ = \rho d\sqrt{k}\mathrm{Re}/\mu$.

The two-layer formulation, with a continuous switch between the two models at a certain distance from the wall, was first proposed in [20] for structured grids. For numerical reasons, a time-derivative is added to the algebraic relation of the one-equation model as $d(\rho\varepsilon)/dt = \mathrm{a}(\rho k^{3/2}/l_\varepsilon - \rho\varepsilon)$. The final ε-equation of TLKE uses a linear blending of the ε-equations of the two models, $\lambda(\varepsilon - \text{eq. of } k-\varepsilon\ ) + (1-\lambda)(\varepsilon - \text{eq. of 1eq}) = 0$, with similarly blended expressions for the dissipation term D_k and the turbulent viscosity. The same function λ as proposed in [20], $\lambda = 0.5\{1 + \tanh[(\mathrm{Re}_d - \mathrm{Re}_d^*)/A]\}$ with $\mathrm{Re}_d = \rho d\sqrt{k}\mathrm{Re}/\mu$ is used. Recommended constant values are $\mathrm{a} = 1, A = 1, \mathrm{Re}_d^* = 150$. The wall boundary conditions are $k_w = 0,\ \varepsilon_w = 0$ whereas at the inflow $k_{in} = 1.5(T_u V_{in})^2$, Tu being the turbulence intensity and $\varepsilon_{in} = c_\mu f_\mu \mathrm{Re}(\rho k_{in}^2/\alpha\mu)$, with $\alpha = \mu_t/\mu = 20$.

It is worth mentioning that the three models described above require the distance d of any internal grid node from the wall. This is simply estimated as the minimum distance of each node from all the wall nodes and segments. In view of these, it becomes evident that the aforemantioned models can be readily implemented on unstructured grids.

3 NUMERICAL SOLUTION METHOD

The Favre-averaged compressible Navier-Stokes equations are discretized on an unstructured grid with triangular elements using a node-centered, finite-volume technique and solved through a time-marching scheme. At each node, the control-volume is defined by successively connecting the midpoints of the edges incident upon the node with the barycenters of the surrounding elements (median-dual tesselation). In an alternative definition of control-volumes, the center of the containment circle of each triangle is used instead of its barycenter (containment-circle tesselation). The latter has been originally proposed by Barth [3] and is highly recommended for finite-volume discretizations on stretched grids, like those used close to the walls.

The time-marching Navier-Stokes solver uses a pointwise-implicit Gauss-Seidel scheme. The Roe [21] approximate Riemann solver [21] is employed for the calculation of the in-

viscid fluxes combined with a MUSCL-extrapolation scheme for higher order accuracy. The primitive variable gradients are computed using an unweighted least-squares technique in order to establish an accurate solution in high aspect-ratio grid cells [22], [15]. Furthermore, the use of the two-dimensional Barth-Jespersen limiter [3], was found absolutely necessary for stability purposes, since the very stretched grid cells near the wall may easily cause local overshoots or even breakdown. A first-order upwind scheme is used for the discretization of the inviscid terms of the turbulence model equation(s). They are handled by the same pointwise solver and solved in a loosely-coupled manner with the mean-flow equations. The viscous terms are calculated by assuming linear distributions of flow quantities in each triangle. The implementation of the low-Reynolds turbulence models requires source terms linearization, as a means to overcome numerical problems caused by their stiffness in regions close to solid walls. For this purpose, the linearization proposed in [17] and [13] was used for SST and SA respectively, while for the TLKE the linearization of the negative part of the source term was used.

4 RESULTS AND DISCUSSION

The aforementioned turbulence models will be tested in the numerical prediction of attached and separated flows over single- and multi-element airfoils. We present the the flow around: (a) the isolated two-element NLR-7301 airfoil and (b) the single-element ONERA A-airfoil, in various flow conditions. In what follows, TR denotes that transition modelling has been used (for example SATR), and FV2 denotes containment circle-dual tesselations (for example TLKEFV2).

4.1 The Two-Element NLR-7301 Airfoil

The NLR-7301 two-element configuration consists of an airfoil (chord C=0.57 m) and a single-slotted trailing edge flap. The flap (of 0.32C length) is staggered at 20 deg with respect to the airfoil and overlaps with it for 0.053C length. Two different configurations will be considered. In the first case, the airfoil-flap gap was equal to 0.013C and the angle of attack 6.1 deg, while in the second case, the gap equals 0.026C and the angle of attack 13.1 deg. For both configurations, experiments have been carried out in the NLR wind-tunnel at Re/C = 2.51x10^6 and M_∞ = 0.185 with free transition [23]. The airfoil-flap configuration is so designed that the flow remains attached, apart from a small laminar separation bubble on the airfoil leading edge.

The unstructured grids used for both cases consist of about 150000 nodes and 300000 triangles. The first node spacing off the wall is of the order of $10^{-6}C$. The finite-volume scheme was applied using the median-dual tesselation. Fully turbulent flow conditions were assumed for the three turbulence models. The CFL number increased linearly from a small initial value to CFLmax within the first NITER iterations. The (CFLmax,NITER) values were (50,200) for the SA model, (20,300) for SST and (10,500) for TLKE, with 15 internal steps were used per Gauss-Seidel iteration. About 10000 iterations were used

for all models, without any other convergence criterion. The results are grid independent and well-converged in terms of flow quantities like the lift or the drag coefficients.

The pressure (C_p) and skin friction (C_f) coefficient distributions along the main airfoil and the flap, as well as the displacement thickness distributions on the airfoil suction side are compared with experimental data, figure 1, for both cases (1.3 % and 2.6 % gap). The C_p comparison in the small gap is excellent for all models, since the flow is attached and the angle of attack is small. In the case of 2.6 % gap, some discrepancies with respect to experimental results appear along the airfoil and flap pressure sides. These discrepancies are more pronounced at the leading-edge and extent along the whole pressure sides. The SA model predicts a better leading-edge pressure peak, but the other two models (SST, TLKE) match closer the experimental distribution after midchord. This is attributed to the fact that the very stretched grid used, in conjuction with the high angle of attack allows for an unphysical amount of artificial dissipation to be introduced into the inviscid fluxes, affecting thus the solution. In accordance to this claim is the fact that the C_f distributions along the pressure side seem to be unaffected. The artificial dissipation issue will be further discussed in the second problem and remedies will be proposed. A totally different performance is noticed in the C_f distributions from the three models along the suction side. In the small gap case, the experimental results are scarce, so it is difficult to draw definite conclusions. In the larger gap, the SST seems to give better predictions. In any case, the SST allows for a more "viscous" solution to evolve, in contrast to the SA model, with the TLKE curves lying between them. This is also verified by the velocity profiles shown in figure 2. Concerning the displacement thickness distributions, they are judged to be satisfactory. It should be mentioned that the boundary layer edge has been computed by the Stock and Haase method [24] and that the post-processing in the unstructured grid is not a trivial task. In figure 2, the parallel to the wall velocity profiles are compared with experimental data. The comparisons concern six measurement stations: two over the rear part of the airfoil pressure side, three along the flap suction side (the lattest at the trailing edge) and one at the flap wake. The overall comparison is judged to be satisfactory. In particular, the SA model seems to be in closer agreement with experiment at the first four stations but, at the last two ones (flap trailing edge and wake), the TLKE predictions outperform the rest. The two first profiles predict a thicker boundary layer, due likely to the assumption of a fully turbulent flow. In addition, all the numerical results in the last figure seem to underestimate the wake mixing procedure, giving thus a clear peak for the flap wake, while in the experiment this peak has been smeared out.

4.2 The ONERA A-Airfoil

In this section, the ONERA A-airfoil (chord C=0.6 m) is analyzed at various flow conditions, with and without transition trip. With the same freestream Mach number ($M_\infty = 0.15$), this airfoil will be investigated initially for a single operating point at Re/C = 2.1x10^6 and $\alpha = 13.3$ deg. As reported in the literature [25], this case exhibits a

small leading-edge separation bubble and trailing-edge turbulent separation. Then, it will be analyzed at ten operating points at a different Reynolds number (Re/C = 3.13x10^6) and angles of attack in the range $\alpha = 3.4 - 17.1$ deg (3.4, 10.1, 12.1, 14.1, 14.6, 15.1, 15.6, 16.1, 16.6, 17.1). A single unstructured grid with approximately 65000 nodes and 130000 triangles has been generated. Close to the solid wall, structured-like node layers are formed, ensuring an approximately constant distance of the first node off the wall of the order of $10^{-6}C$. The undertaken grid-dependency study is not included in this paper.

Using the three models (SA, SST and TLKE) in their standard form, the flow field was computed at the first operating point. Figure 3 illustrates pressure and friction coefficients (C_p and C_f) as well as displacement thickness distributions over the airfoil. The left column corresponds to the median-dual tesselation (first finite-volume definition or FV1, this abbreviation is ommitted in the figures) whereas the right column corresponds to the containment circle-dual tesselation (FV2). Results are compared with each other and with experimental data. Unfortunately, C_f data in the front part of the suction side, where most differences between models are located, are not available. From the C_p plots, two conclusions can be drawn, which will be reconfirmed elsewhere. The first conclusion is that all used models produce similar pressure distributions, for the same tesselation. The second conclusion is that the FV2 scheme has greatly affected the overall performance, matching perfectly the experimental C_p peak. However, FV2 produces slight discrepancies very close to the trailing edge, probably associated with the pressure peak at the suction leading edge. The latter is a consequence of the change in airfoil circulation that occurs when the bubble-type separation is underpredicted in size (more pronounced in SST model). Concerning C_f predictions, the SA and TLKE models produce similar, though not identical, distributions which are in good agreement with measurements. As in the NLR case, the SST predicts a more "viscous" solution. Some differences occur in the displacement thickness predictions, where the SA results seem to be generally closer to the experiments, especially in the FV2 case, but this will be discussed below where the transverse velocity profiles are shown.

For the same operating point, figure 4 presents a more extensive view of the predictive capabilities of the SA model, using four variants of the solution software (transition model or not, FV1 or FV2). Transition is imposed at 0.30C on the pressure side, a location known from the experiments; on the suction side, a transition trip at 0.12C was arbitrarily set. Transition on the suction side can be readily observed from the corresponding C_f curves. The pressure distribution on the suction side, close to the leading edge, shows that the incorporation of a transition model to the FV2 tesselation does not improve the results which are already very close to the experimental data. On the contrary, it yields a high negative local pressure peak, which points to a local laminar flow with well controlled artificial diffusion effects. The displacement thickness plot is also in favour of SAFV2 which is quite accurate by itself, without resorting to transition modelling.

Figures 6, 7 and 8 compare transverse non-dimensional velocity profiles at twelve axial positions along the suction side and three stations along the wake, close to the trailing

edge. The following comments correspond to figure 6 and concern results obtained using the median-dual tesselation. Quite early, the SA model shows its tendency to create a separated flow region. This appears first at about 70 percent of chord. The turbulent separated flow profile at the very last position on the airfoil, predicted using SA, comes too close to the measured one. The other two models (especially the SST one) fail to predict separation. On the other hand, the SA model, with the first tesselation, overpredicts both the extent and thickness of separation. In the wake, SA matches the experimental curves close to the trailing edge but fails to reproduce the correct peak due to flow mixing further downstream.

As expected, the FV2 tesselation, figure 7, improves the accuracy of the predictions close to the wall where the grid cells are very stretched. It is noticeable that the SAFV2 distribution is in excellent agreement with measurements in the major part of the airfoil. However, in contrast to what was obtained using FV1, the turbulent separation close to the trailing edge is underestimated. Furthermore, with the FV2 tesselation, SAFV2 is the only model that predicts a separated flow region. In the wake and close to the airfoil, it underestimates the velocity profile peak which is an immediate consequence of the underestimation of the flow separation in the last part of the airfoil. Further downstream, the velocity patterns are recovered. The results from the other two models are worsen as far as the tendancy for separation is of concern, in comparison with the corresponding FV1 calculations.

The agreement of SA predictions with measurements motivated a further investigation of this model. The outcome of an investigation including transition modelling with SA (coupled with both FV1 and FV2) is shown in figure 8. Two out of the four shown curves (namely SA and SAFV2) are the same as in the previous figures. To these, the SATR and SATRFV2 predictions have been added. By enforcing transition trip, the tendency of the model to predict a large separation zone is controlled. The separation zone entent is reduced by adding the transition model to either SA or SAFV2. However, the combined use of transition and FV2 seems to underestimate the size of separation. Concerning the wake, the general conclusion is that all the three variants of the standard SA configuration lead to an overall improved performance compared to SA.

Results from the various numerical predictions of the flow around A-airfoil, at various inlet flow angles, are shown in figures 5, 9 and 10. For each operating point, four variants of the software (two tesselation techniques, with and without transition modelling) are employed, all with the SA model. Lift (C_l) and drag (C_d) polars are shown in figure 5. As one may observe, the FV2 tesselation leads, generally, to the more accurate results. The transition modelling seems to alter the C_l and C_d distributions towards higher C_l and lower C_d values. Although FV2 significantly improves the SA curve, transition modelling in SA does not result in any visible gain. However, transition modelling introduced into SAFV2 produces the best overall performance. In the C_l region corresponding low angles of attack, all models produce satisfactory results.

Six out of the ten operating points are further analyzed in figure 9. At all six angles

of attack, the pressure side C_p distribution is accurately captured, regardless the variant used. Differences appear on the suction side, where at higher incidences, FV2 clearly becomes superior in terms of accuracy in the pressure distributions.

Figure 10 presents the C_f distributions for the same cases where the effect of transition modelling on the accurate prediction of friction over the suction side of the airfoil at midchord can be evaluated especially for the higher angles of attack. In the lower angles, the effect of transition is less pronounced. However, it should be pointed out that the transition point on the suction side is considered to be at the same (arbitrary) position irrespective of the flow angle.

As a conclusion, at pre-stall conditions (high angles of attack), the SATRFV2 variant outperforms the other ones, while at the post-stall region the situation becomes not so clear. At lower flow angles, the FV2 option seems to be much more efficient than the incorporation of transition modelling.

4.3 Conclusions

The main conclusions drawn from the numerical study of subsonic high-lift airfoils with one- and two-equation low-Reynolds turbulence models on unstructured grids are: (a) for the accuracy of the numerical solution on stretched grids, using least-squares approximation for the gradients of the flow variables and the Barth-Jespersen limiter are required, (b) in case of high angles of attack, the solution accuracy is maintained only by employing the containment circle-dual tesselation, (c) the SA model was found to have an overall superior performance compared with SST and TLKE and (d) the inclusion of transition modelling in the calculation is generally outperformed by the use of FV2, but in case of high angles of attack its use over and above FV2 becomes necessary.

Acknowlegments Part of this work has been motivated by the FLOWNET Thematic Network. The authors are grateful to Dr. Werner Haase for providing them with experimental data.

References

[1] Launder B. E. and Sharma B. I., Application of the Energy Dissipation Model of Turbulence to the Calculation of Flow Near a Spinning Disc, *Letters in Heat and Mass Transfer*, **1**, 2, 131-138, (1974).

[2] Chien K.-Y., Predictions of Channel and Boundary-Layer Flows with a Low-Reynolds-Number Turbulence Model, *AIAA J.*, **20**, 1, 33-, (1982).

[3] Barth T. J., Numerical Aspects of Computing Viscous High Reynolds Number Flows on Unstructured Meshes, *AIAA Paper 91-0721*, (1991).

[4] Farhat C. and Lanteri S., Simulation of Compressible Viscous Flows on a Variety of MPPs: Computational Algorithms for Unstructured Dynamic Meshes and Performance Results, *Comp. Meth. in Appl. Mech. and Eng.*, **119**, 35-60, (1994).

[5] Jameson A. and Mavriplis D. J.,Finite Volume Solution of the Two-Dimensional Euler Equations on a Regular Triangular Mesh, *AIAA J.*, **24**, 611-618, (1986).

[6] Mavriplis D. J., Jameson A. and Martinelli L., *Multigrid Solution of the Navier-Stokes Equations on Triangular Meshes*, ICASE Report 89-11, (1989).

[7] Mavriplis D. J., Algebraic Turbulence Modelling for Unstructured and Adaptive Meshes, *AIAA J.*, **29**, 12, 2086-2093, (1991).

[8] Pan D., Cheng J-C., Upwind Finite-Volume Navier-Stokes Computations on Unstructured Triangular Meshes, *AIAA J.*, **31**, 9, 1618-1625, (1993).

[9] Mavriplis D. J. and Martinelli L., Multigrid Solution of Compressible Turbulent Flow on Unstructured Meshes Using a Two-Equation Model, *Int. J. for Num. Meth. in Fluids*, **18**, 887-914, (1994).

[10] Mohammadi B. and Pironneau O., *Analysis of the $k-\varepsilon$ Turbulence Model, Research in Applied Mathematics*, Series Editors: P. G. Ciarlet and J. L. Lions, John Willey & Sons, (1994).

[11] Kasbarian C., Lebigre O., Mallet M., Mantel B., Ravachol M. and Tentillier M., Development of a Finite Element Navier-Stokes Solver Using Unstructured Adapted Grids. Applications to Turbulent Flows, in *Computational Fluid Dynamics '92*, **1**, 229-236, Ch. Hirsch et al. (Editors), (1992).

[12] Jacon F. and Knight D., A Navier-Stokes Algorithm for Turbulent Flows Using an Unstructured Grid and Flux Difference Splitting, *AIAA Paper 94-2292*, (1994).

[13] Spalart P. and Allmaras S., A One-Equation Turbulence Model for Aerodynamic Flows, *AIAA Paper 92-0439*, (1991).

[14] Baldwin B. S. and Barth T. J., A One-Equation Turbulence Transport Model for High Reynolds Wall-Bounded Flows, *AIAA Paper 91-0610*, (1991).

[15] Anderson W. K., Bonhaus D. L., An Implicit Upwind Algorithm for Computing Turbulent Flows on Unstructured Grids, *Computers Fluids*, **23**, 1, 1-21, (1994).

[16] Barth T. J., Aspects of Unstructured Grids and Finite-Volume Solvers for the Euler and Navier-Stokes Equations, in *VKI Lecture Series 1990-03, Computational Fluid Dynamics*, March 21-25, (1994).

[17] Menter F. R., Zonal Two Equation $k-\omega$ Turbulence Models for Aerodynamic Flows, *AIAA Paper 93-2906*, (1993).

[18] Launder B.E. and Spalding D.B., The Numerical Computation of Turbulent Flows, *Comp. Meth. in Appl. Mech. and Eng.*, **103**, 456-460, 1974.

[19] Wolfshtein M., The Velocity and Temperature Distribution in One-Dimensional Flow with Turbulent Augmentation and Pressure Gradient, *Int. J. of Heat and Mass Transfer*, **12**, 301-318, (1969).

[20] Jongen T. and Marx Y., An Efficient and Robust Numerical Method for Simulating Turbulent Fluid Flows, in *Computational Fluid Dynamics '96*, 366-373, John Wiley and Sons Ltd., (1996).

[21] Roe P., Approximate Riemann Solvers, Parameter Vectors, and Difference Schemes, *J. of Comp. Phys.*, **43**, 357-371, (1981).

[22] Barth T. J., Aspects of Unstructured Grids and Finite-Volume Solvers for the Euler and Navier-Stokes Equations, in *AGARD Report 787, Special Course on Unstructured Grid Methods for Advection Dominated Flows*, (1992).

[23] Van den Berg B, *Boundary Layer Measurements on a Two-Dimensional Wing with Flap*, National Aerospace Lab., NLR TR 79009 U, Amsterdam, The Netherlands, (1979).

[24] Stock H.W. and Haase W., Determination of length scales in Algebraic Turbulence Models for Navier-Stokes Methods, *AIAA J.*, **27**, 1, 5-14, (1989).

[25] Haase W., Chaput E., Elsholz E, Leschziner M.A. and Mueller U.R. (editors), ECARP-European Computational Aerodynamics Research Project: Validation of CFD Codes and Assessment of Turbulence Models, *Notes on Numerical Fluid Mechanics*, **58**, Vieweg Verlag, (1996).

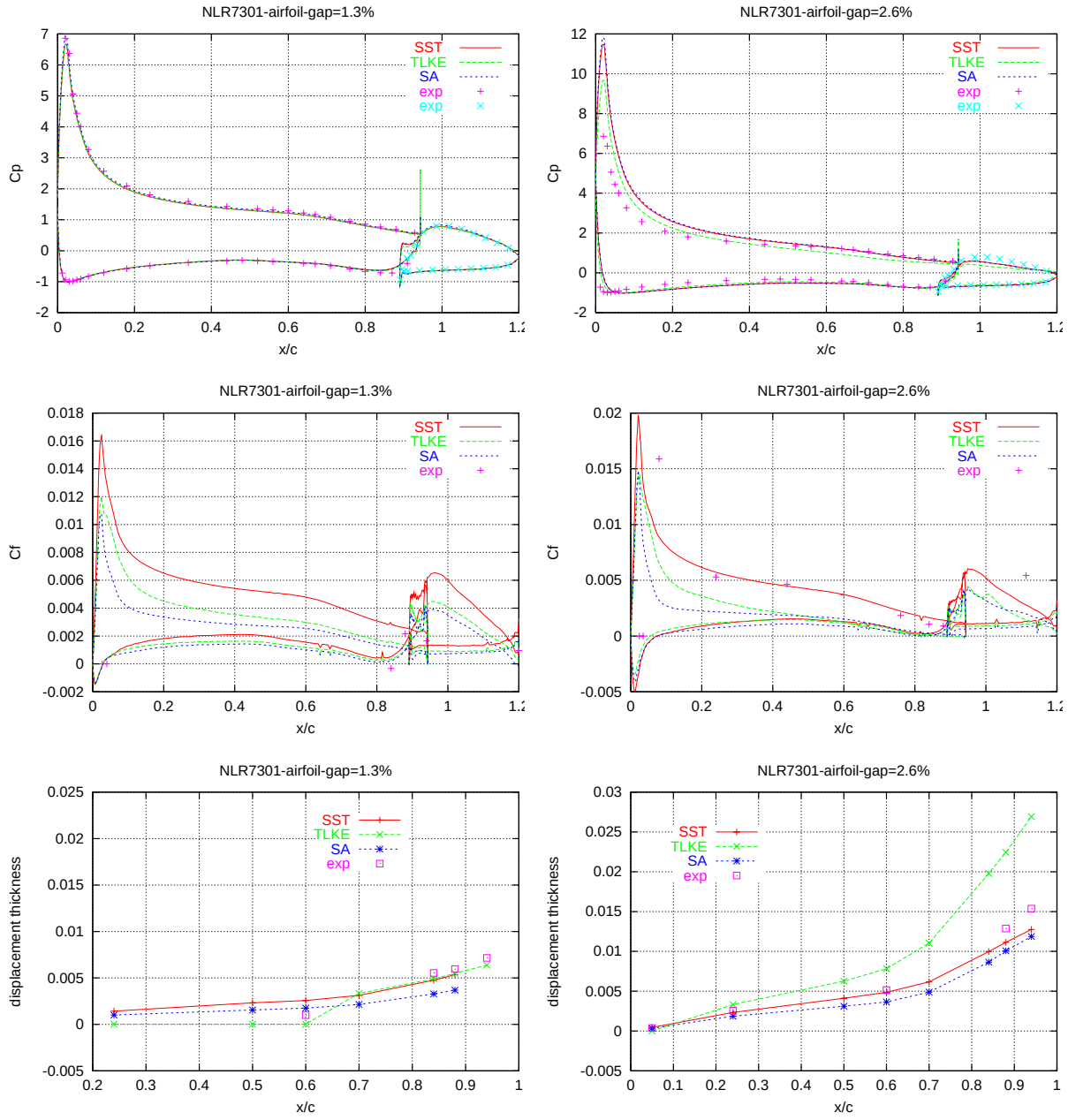

Figure 1: Pressure and skin friction coefficients along the main airfoil and flap for the NLR case. Dislacement thickness along the main airfoil suction side. Left: 1.3 %C gap case. Right: 2.6 %C gap case.

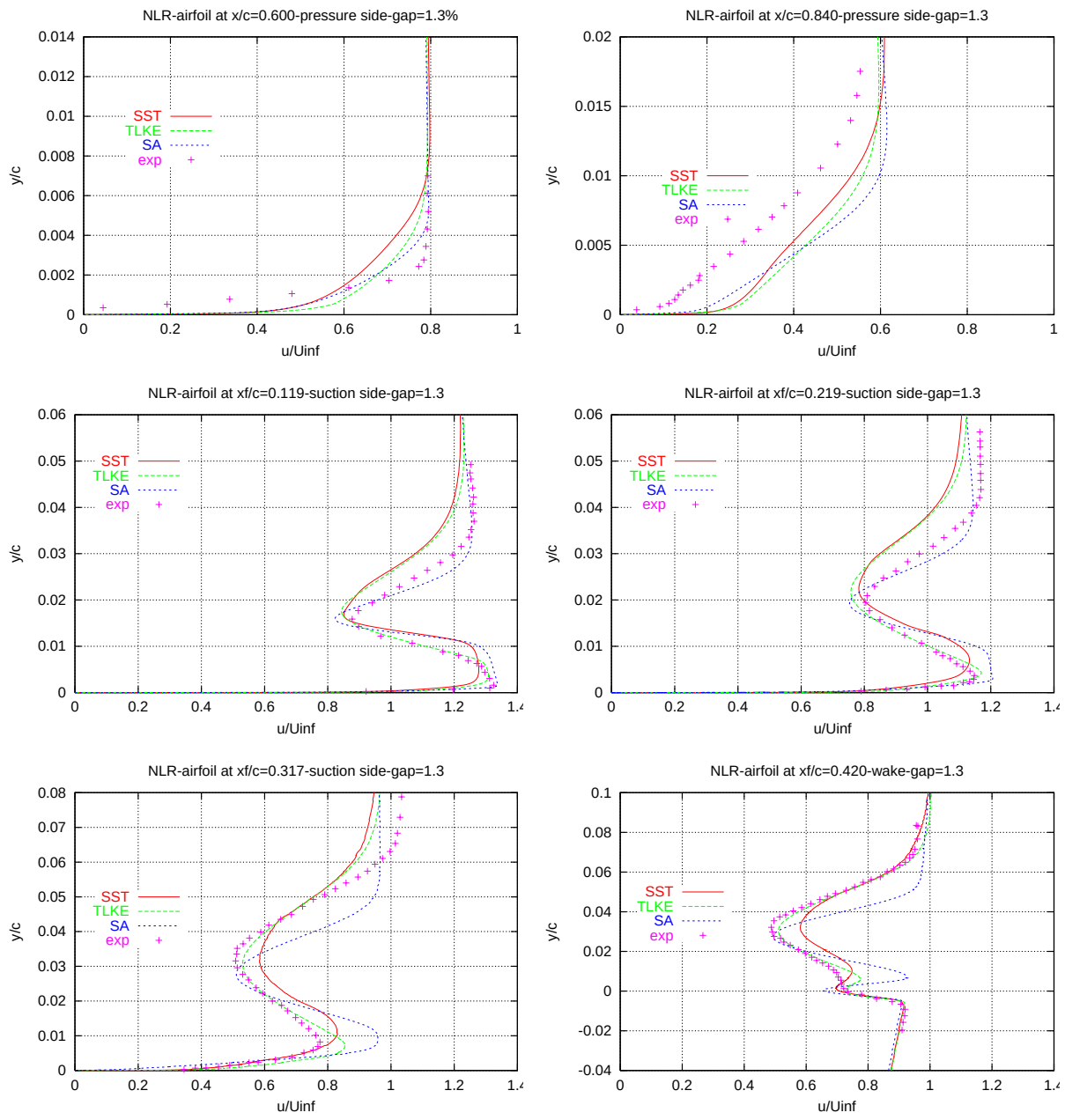

Figure 2: NLR-1.3 %C case: U/U_∞ velocity profiles, (U parallel to the wall), for six different stations along the main wing and flap.

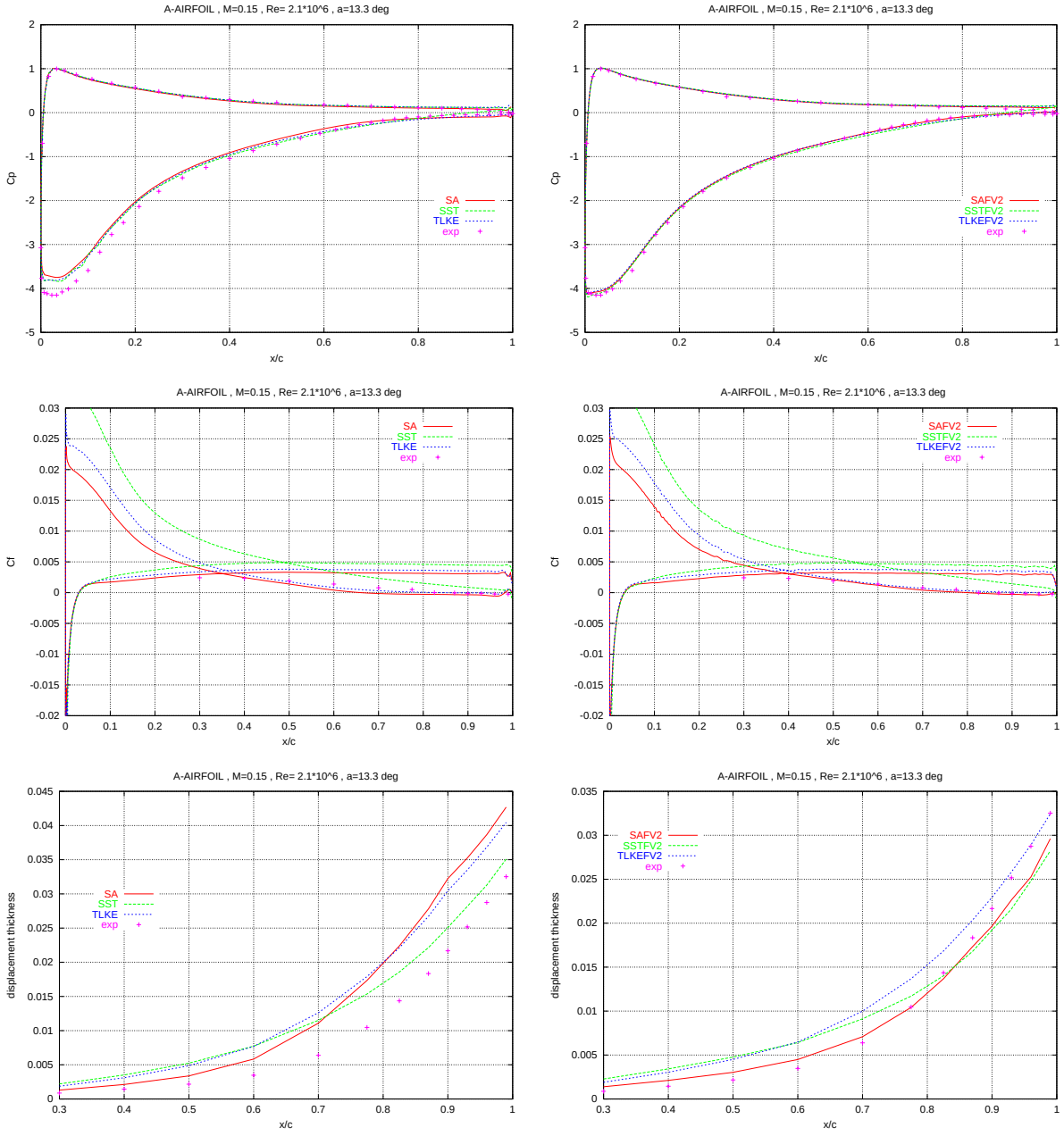

Figure 3: A-airfoil, first operating point: Pressure, skin friction coefficient and displacement thickness distributions along the airfoil. Results from the three turbulence models. No transition modelling neither FV2 has been used. Left: Median-dual tesselation of the domain. Right: Containment-circle tesselation of the domain.

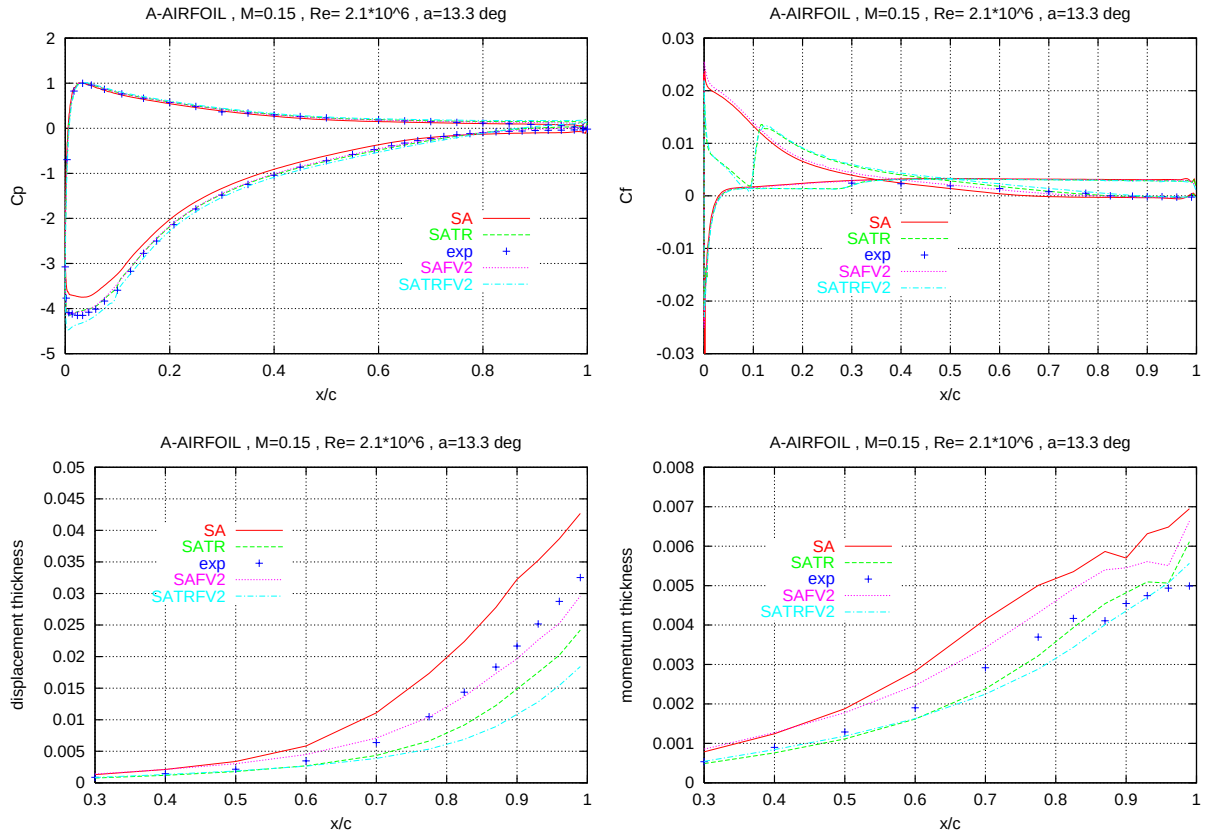

Figure 4: A-airfoil, first operating point: Pressure, skin friction coefficients and displacement, momentum thickness distributions along the airfoil. Results from the SA model with/without transition modelling-FV1/FV2.

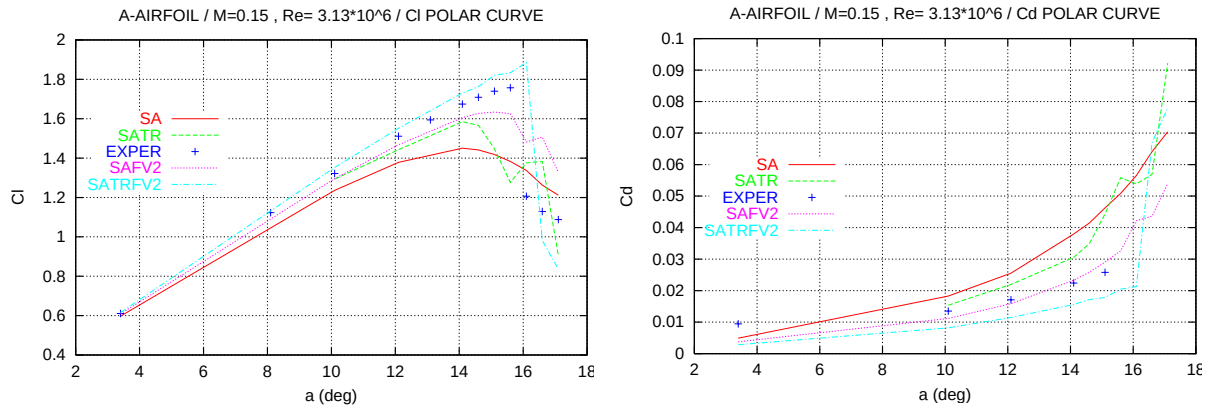

Figure 5: A-airfoil, multiple operating points: Lift and drag coefficient polar curves.

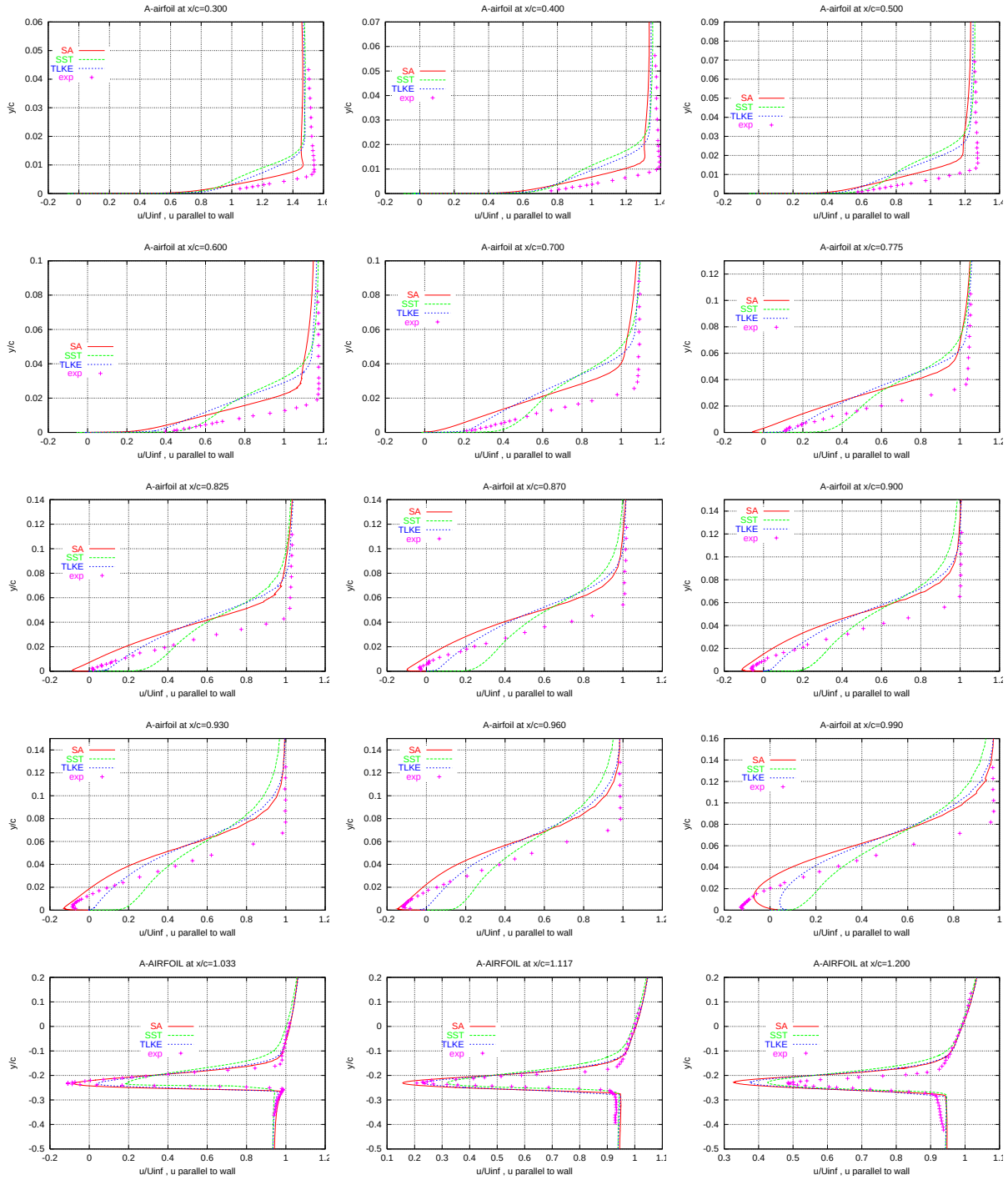

Figure 6: A-airfoil, first operating point: U/U_∞ velocity profiles, (U parallel to the wall) along the airfoil suction side and wake. Results from the three turbulence models. No transition modelling neither FV2 has been used.

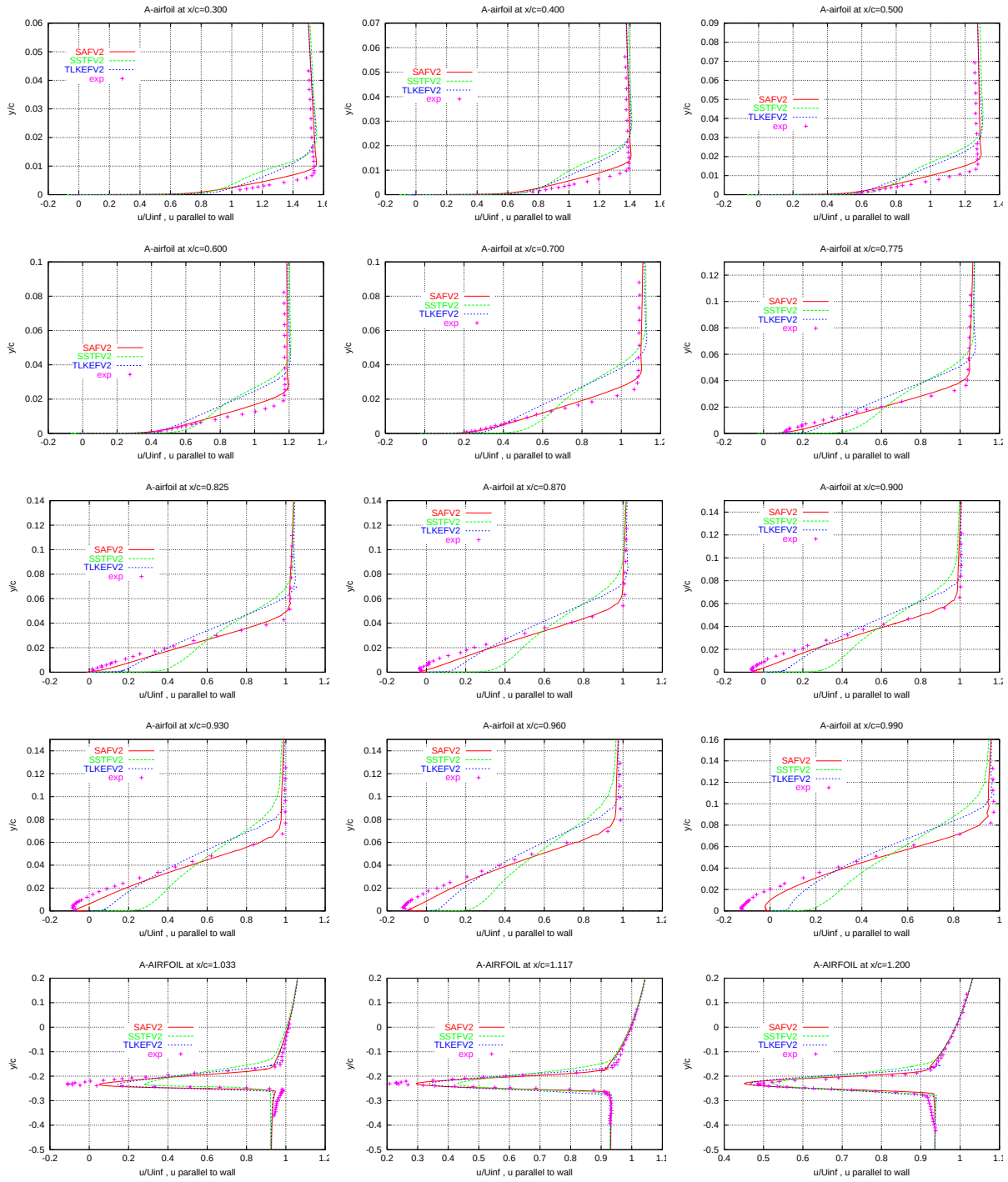

Figure 7: A-airfoil, first operating point: U/U_∞ velocity profiles, (U parallel to the wall) along the airfoil suction side and wake. Results from the three models. FV2 has been used but no transition modelling.

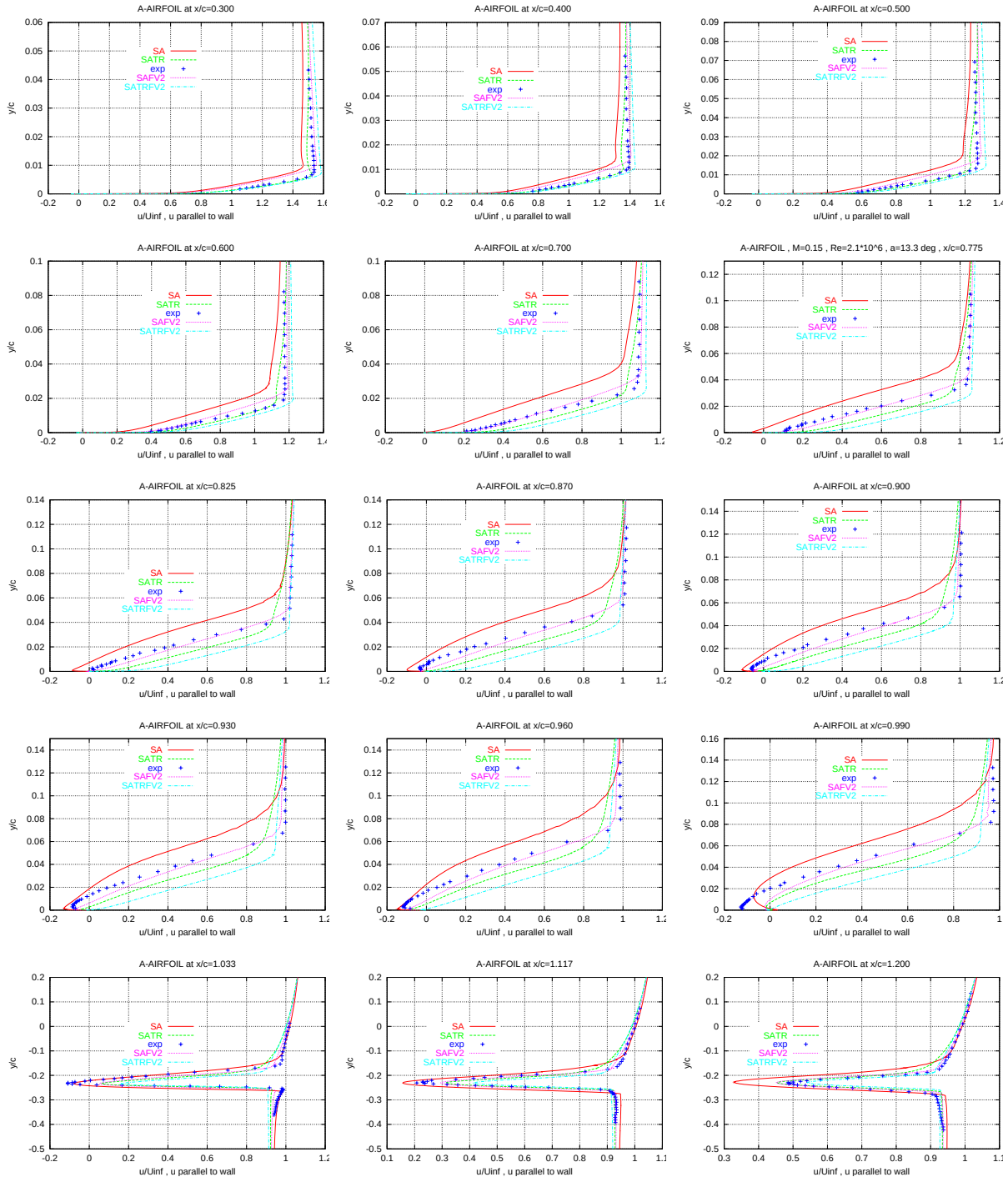

Figure 8: A-airfoil, first operating point: U/U_∞ velocity profiles, (U parallel to the wall) along the airfoil suction side and wake. Results from the SA model with/without transition modelling-FV1/FV2.

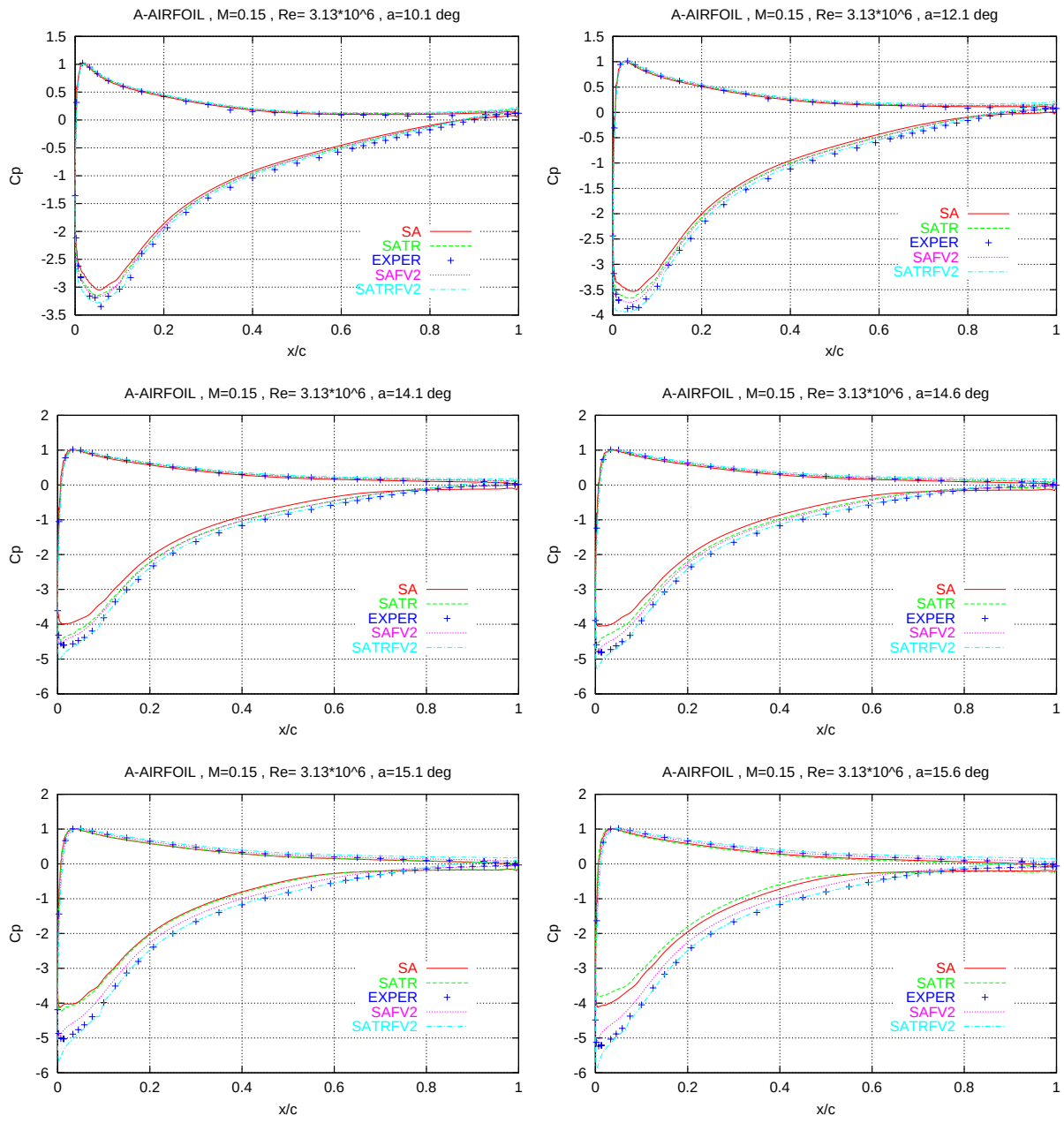

Figure 9: A-airfoil, multiple operating points: Pressure coefficient distributions along the airfoil for different incidence angles. Results from the SA model with/without transition modelling-FV1/FV2.

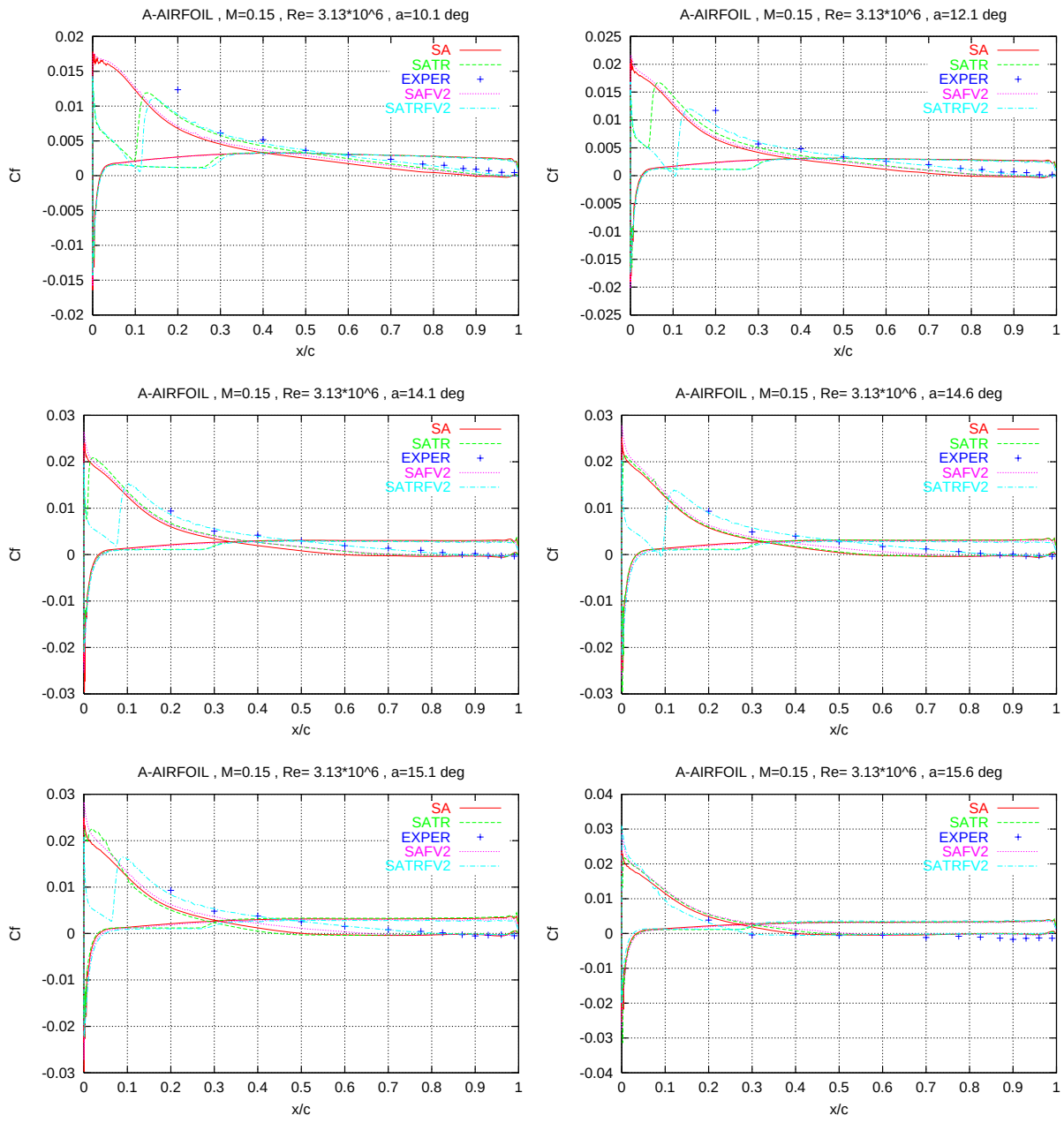

Figure 10: A-airfoil, multiple operating points: Skin friction coefficient distributions along the airfoil for different incidence angles. Results from the SA model with/without transition modelling-FV1/FV2.